New Occurrence of Rusinovite, $Ca_{10}(Si_2O_7)_3Cl_2$: Composition, Structure and Raman Data of Rusinovite from Shadil-Khokh Volcano, South Ossetia and Bellerberg Volcano, Germany

Dorota Środek [1],* , Rafał Juroszek [1] , Hannes Krüger [2] , Biljana Krüger [2] , Irina Galuskina [1] and Viktor Gazeev [3,4]

1   Department of Geochemistry, Mineralogy and Petrography, Faculty of Earth Sciences, University of Silesia, Będzińska 60, 41-200 Sosnowiec, Poland; rjuroszek@us.edu.pl (R.J.); irina.galuskina@us.edu.pl (I.G.)
2   Institute of Mineralogy and Petrography, University of Innsbruck, Innrain 52, 6020 Innsbruck, Austria; hannes.krueger@uibk.ac.at (H.K.); biljana.krueger@uibk.ac.at (B.K.)
3   Insitute of Geology of Ore Deposits, Petrography, Mineralogy and Biochemistry, RAS, Staromonetny 35, 119017 Moscow, Russia; gazeev@igem.ru
4   Vladikavkaz Scientific Centre of the Russian Academy of Sciences, Markov str. 93a, 362008 Vladikavkaz, Republic of North Ossetia-Alania, Russia
*   Correspondence: dsrodek@us.edu.pl; Tel.: +48-693-404-979

Abstract: Rusinovite, $Ca_{10}(Si_2O_7)_3Cl_2$, was found at two new localities, including Shadil-Khokh volcano, South Ossetia and Bellerberg volcano, Caspar quarry, Germany. At both of these localities, rusinovite occurs in altered carbonate-silicate xenoliths embedded in volcanic rocks. The occurrence of this mineral is connected to specific zones of the xenolith characterized by a defined Ca:Si < 2 ratio. Chemical compositions, as well as the Raman spectra of the investigated rusinovite samples, correspond to the data from the locality of rusinovite holotype—Upper Chegem Caldera, Northern Caucasus, Russia. The most intense bands of the Raman spectra are related to vibrations of (Si_2O_7) groups. Unit cell parameters of rusinovite from South Ossetia are: a = 3.76330(4) Å, b = 16.9423(3) Å, c = 17.3325(2) Å, V = 1105.10(4) Å^3, Z = 2. The performed synchrotron radiation diffraction experiments did not confirm a doubling of c as reported for the synthetic phase, $Ca_{10}(Si_2O_7)_3Cl_2$. However, one-dimensional diffuse scattering parallel to $\mathbf{b}^*$ has been observed. This can be interpreted with an ordered arrangement of Si_2O_7 groups creating layers with a doubled a parameter. Consequently, the two different displacements of neighbouring layers allow random stacking faults to occur.

Keywords: Rusinovite; Raman spectroscopy; pyrometamorphism; stacking faults; Shadil-Khokh volcano; Bellerberg volcano

1. Introduction

Rusinovite, $Ca_{10}(Si_2O_7)_3Cl_2$, was found in 2011 in an altered carbonate-silicate xenolith from the Upper Chegem Caldera located in Kabardino-Balkaria, Northern Caucasus, Russia. These rocks are formed at high-temperature and low-pressure conditions (sanidinite facies) and contain different Cl-bearing minerals, such as rondorfite $MgCa_8(SiO_4)_4Cl_2$, rustumite $Ca_{10}(SiO_4)(Si_2O_7)_2Cl_2(OH)_2$, and minerals of the mayenite supergroup: wadalite $Ca_{12}Al_{10}Si_4O_{32}Cl_6$ and chlorkyuygenite $Ca_{12}Al_{14}O_{32}[(H_2O)_4Cl_2]$ [1–3]. Besides their natural occurrence, rusinovite-type synthetic phases were also described from anthropogenic formations. Firstly, it was reported from the combustion

ashes comprised by Cl-bearing Ca-silicates, which were formed after the incineration of waste [4]. Secondly, the $Ca_{10}(Si_2O_7)_3Cl_2$ phase was also described as "chesofiite" from the burned spoil heaps of the coal mine located near the town of Kopeisk, Chelyabinsk Region, Russia [5]. In addition to the geological and anthropogenic occurrences, a phase with rusinovite composition and structure was also synthesized utilizing the flux method [6]. A new green-emitting phosphor was created by doping the synthetic analogue of rusinovite with Europium ($Ca_{10}(Si_2O_7)_3Cl_2$:Eu^{2+}) [7]. Its emission is efficiently excited by the output of near-UV light-emitting diodes (LEDs).

Both rusinovite and the synthetic analogue are reported as strongly elongated grains, which form needle-like single crystals or spherulites composed of fibrous aggregates [1,6]. The structure of the synthetic phase was primarily reported as order-disorder (OD) structure with an orthorhombic unit cell [6], but later its structure was redefined as monoclinic [4]. Galuskin et al. [1] have described the structure of rusinovite as columns of disordered "face-sharing" disilicate units extending parallel to **a**. At a local level, only each second Si_2O_7 unit (along **a**) can be occupied in the structure. Due to the small dimensions of the grains from the holotype locality, some structural issues were still unresolved (such as possible superstructures due to the ordering of the Si_2O_7 groups).

The main goal of this study is to describe rusinovite from two new localities, including chemical composition and Raman spectroscopy. Furthermore, the structure of rusinovite from South Ossetia is to be re-investigated using synchrotron radiation, to check for superstructures, which have been observed in synthetic analogues.

2. The Occurrence and Paragenesis of Rusinovite

Rusinovite was found in pyrometamorphic rock at the two localities. The first one is Shadil-Khokh volcano, belonging to the Kel'sky volcanic plateau located at the southern part of the Greater Caucasus Mountain Range in Southern Ossetia. Small (about 2 m in diameter) altered carbonate-silicate xenolith was revealed at the north-west slope of the volcano within dacite lava.

This xenolith is composed of minerals characteristic for sanidinite facies, such as spurrite, larnite, gehlenite, merwinite, bredigite, rondorfite, and srebrodolskite [8]. Rusinovite occurs as relatively large (100–200 μm in length) elongated crystals with a characteristic macroscopic brown-orange colour in small veins (up to 0.5 cm wide) encountered at the exocontact zone of xenolith (Figure 1A,B). In these zones, another Cl-bearing phase–eltyubyuite, $Ca_{14}Fe^{3+}_{10}Si_4O_{32}Cl_6$, was noted [9]. Rusinovite was found also at the endocontact zone of strongly altered dacite (Figure 2A,B).

The presence of microzonation at both endo- and exocontact zones is reflected in the zonal distribution of minerals with the different Ca:Si ratio. At the endocontact, rock is presented by dacite microbreccia and carbonate-silicate microxenoliths (Figure 2A,B). We distinguish the following zonation (Figure 2C). The first zone (the numbering is according to the Ca:Si ratio increasing)–dacite, consisting of enstatite, albite phenocrysts, and quartz enclosed in the fine-grained aggregate of diopside, plagioclase, and Na–K feldspar. Visible zonation of enstatite (Figure 2C) is caused by variations of minor Fe substitutions in composition. Ilmenite occurs as an accessory mineral. The second zone is composed of massive gehlenite. The third zone is comprised mostly of rusinovite and gehlenite; hydroxylellestadite and wollastonite are noted rarely. The fourth zone is represented by strongly altered rock, mainly composed of secondary Ca–Si hydrosilicates, rusinovite, cuspidine and rondorfite.

Another type of zonation is observed at the dacite-xenolith (exocontact) boundary (Figure 1A,B). The altered dacite is composed of diopside, enstatite, plagioclase phenocrysts, and quartz. The matrix is presented by a fine-grained aggregate of plagioclase. Furthermore, ilmenite, titanite, apatite, and pyrite occur as accessory minerals. The next zone towards xenolith, contains Al–Ca hydrosilicates (Figure 1C). In the second zone, wollastonite and andradite are the main minerals. The accessory phases are represented by cuspidine, gehlenite, and wadalite. In the third zone, rusinovite occurs as a major component together with cuspidine. Wollastonite is present, but not as commonly as in the previous zone. Cl-bearing hydroxylellestadite, gehlenite, magnesioferrite, and rondorfite are also noted. The last

zone is a strongly altered xenolith part composed mostly of secondary Ca-hydrosilicates with the relics of rondorfite, larnite, cuspidine, and merwinite.
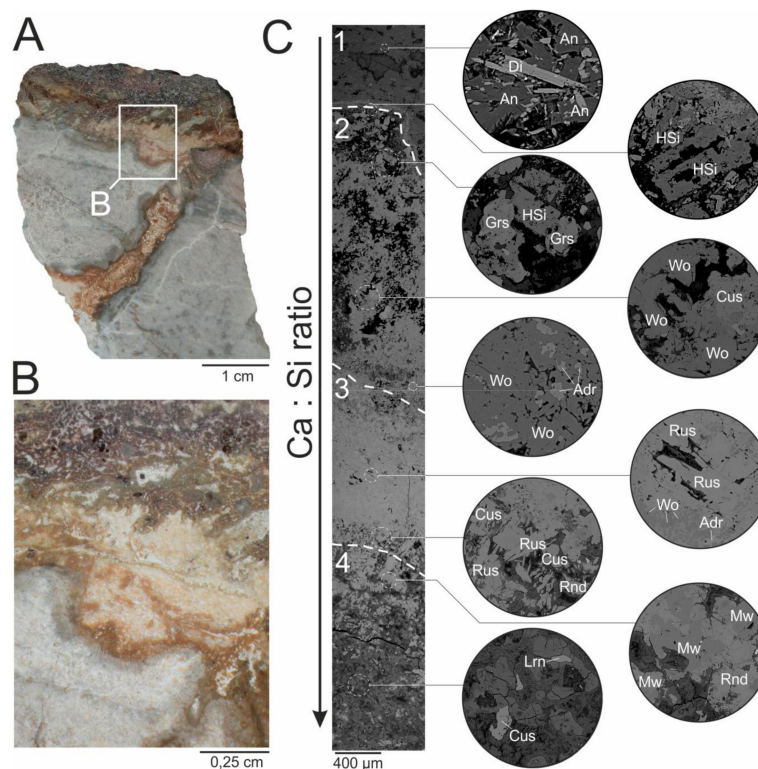

Figure 1. (**A**,**B**) Macroscopic image of exocontact; (**C**) BSE (backscattered electron) image of the exocontact zone; 1—dacite zone; 2—wollastonite zone; 3—cuspidine—rusinovite zone; 4—altered xenolith. An—anorthite, Adr—andradite, Cus—cuspidine, Di—diopside, Grs—grossular, HSi—Al–Ca hydrosilicates, Lrn—larnite, Mw—merwinite, Rnd—rondorfite, Rus—rusinovite, Wo—wollastonite.

The Bellerberg volcano (Caspar quarry), located near Mayen in the Eifel district in western Germany is the second studied rusinovite locality. In the active quarry, within leucite tephrite, small Ca-rich xenoliths can be found [10]. These xenoliths were formed under similar conditions as the xenoliths from South Ossetia—at high temperatures and low pressure. Bellerberg volcano is a holotype locality for a few Cl-bearing minerals, such as rondorfite $Ca_8Mg[SiO_4]_4Cl_2$ [10], chlormayenite $Ca_{12}Al_{14}O_{32}[\square_4Cl_2]$ [11,12] or vondechenite $Cu_4CaCl_2(OH)_8 \times 4H_2O$ [13].

Macroscopically, the studied xenolith is dark green-grey and contains veins characterized by a colour that is definitely lighter (Figure 3A).

The main part of the xenolith is composed of larnite, gehlenite, rondorfite, Cl-bearing hydroxylellestadite, spurrite, and secondary Ca-hydrosilicates. Perovskite, hematite, cuspidine, Zr-garnet (with a chemical composition close to kerimasite), andradite, and pyrite with chalcopyrite intergrowths are also identified here. The lighter part of the rock is characterized by similar paragenesis, the difference is in the predominance of hydrocalumite among secondary Ca-hydrosilicates. Besides the minerals mentioned above, this zone contains rusinovite, wollastonite, chalcopyrite, baghdadite, and lakargiite (Figure 3B). Aggregates of rusinovite can reach up to 200 µm in size. They contain a lot of mineral inclusions composed of secondary Ca-hydrosilicates, gehlenite, chlorine-bearing ellestadite, perovskite and hematite, mainly, and strongly hydrated zones (Figure 3B).
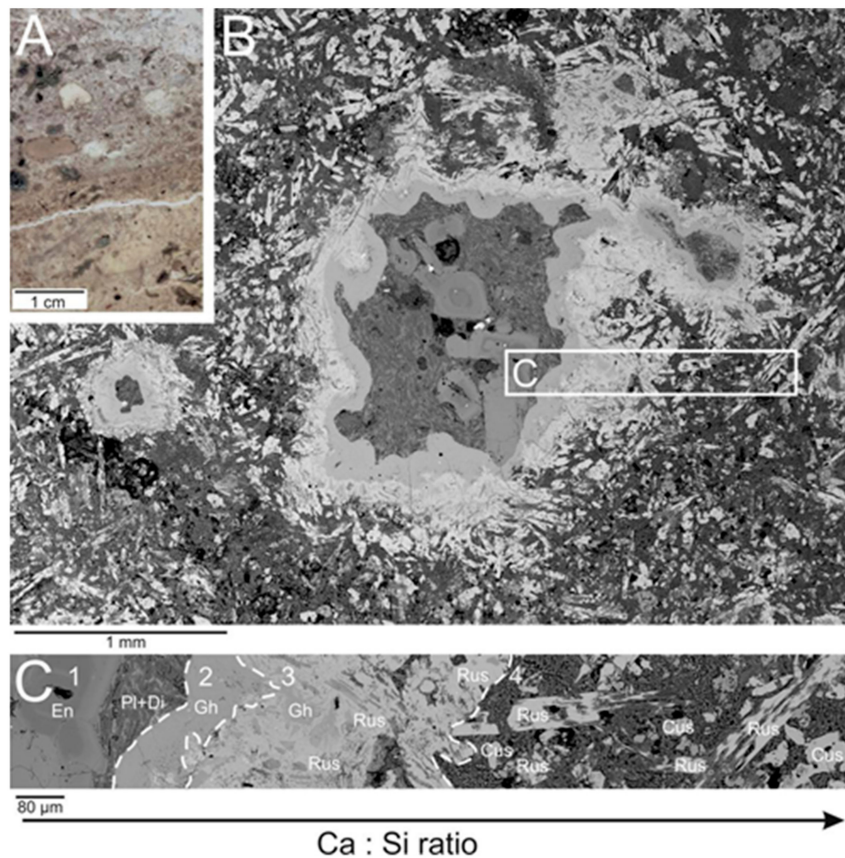
Figure 2. (**A**) Macroscopic image of the endocontact zone; (**B**) BSE image of the endocontact zone; fragment in the frame is magnified in (**C**); Zones: 1—altered dacite zone; 2—gehlenite zone; 3—rusinovite zone; 4—altered xenolith. Cus—cuspidine, Di—diopside, En—enstatite, Gh—gehlenite, Pl—plagioclase, Rus—rusinovite.
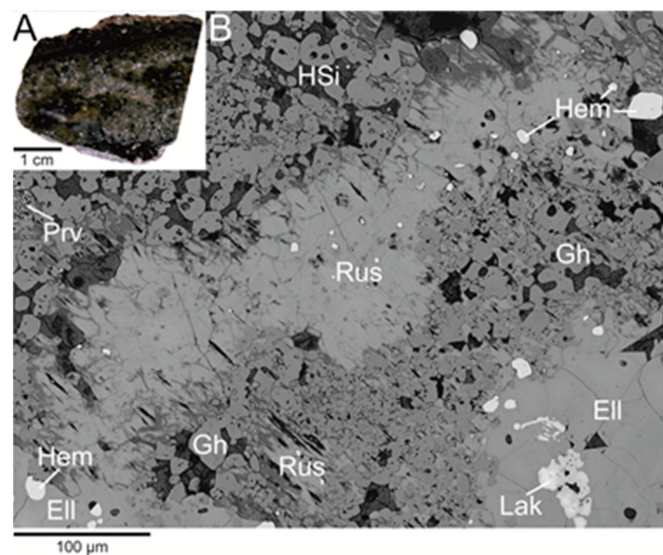

Figure 3. (**A**) Macroscopic photo of vein containing rusinovite from the Bellerberg volcano, Caspar quarry; (**B**) BSE image of rusinovite. Ell—ellestadite, Gh—gehlenite, Hem—hematite, HSi—unidentified secondary Ca-silicates; Lak—lakargiite; Prv—perovskite, Rus—rusinovite.

3. Materials and Methods

The chemical composition and morphology of rusinovite and associated minerals were examined using a scanning electron microscope, the Phenom XL, PhenomWorld (ThermoFisher Scientific, Eindhoven, The Netherlands) equipped with an energy-dispersive X-ray spectroscopy (EDS) detector (Faculty of Earth Sciences, University of Silesia, Sosnowiec, Poland), and a CAMECA SX100 electron microprobe (Institute of Geochemistry, Mineralogy and Petrology, University of Warsaw, Warsaw, Poland). The microprobe analyses were performed at 15 kV and 10 nA using a 1-5 μm beam spot. The following lines and standards were used for rusinovite analyses: Ca$K\alpha$, Si$K\alpha$, Mg$K\alpha$-diopside; Fe$K\alpha$-synthetic Fe_2O_3; Mn$K\alpha$-rhodonite; Ti$K\alpha$-rutile; Cl$K\alpha$-tugtupite.

The Raman spectra of rusinovite and associated minerals were collected using a WITec confocal Raman microscope CRM alpha 300, WITec, Ulm, Germany (Institute of Physics, University of Silesia, Poland) equipped with an air-cooled solid-state laser (λ = 532 nm) and an electron multiplying charge-coupled device (EMCCD) detector. Raman scattered light was focused onto a multi-mode fiber (50 mm diameter) and monochromator with a 600 line/mm grating. An air Olympus MPLAN 100× objective was used. The spectra were collected with an integration time of 100 ms per spectrum and accumulation of 10 scans, precision of ± 1 cm^{-1} and a resolution of 3 cm^{-1}. The laser radiation power was 10mW at the sample and 1 μm diameter of the incident laser beam. The calibration of the monochromator was held by checking the position of the Si (520.7 cm^{-1}). Spectra processing, such as baseline correction and smoothing, was performed using the Spectracalc software package GRAMS (Galactic Industries Corporation, Salem, NH, USA). The band fitting was done using a Gauss-Lorentz cross-product function, with the minimum number of component bands used for the fitting process.

Diffraction data were collected at the X06DA beamline at the Swiss Light Source (Paul Scherrer Institute, Villigen, Switzerland) using a Pilatus 2M-F detector at a distance of 80 mm from the sample. A single 180° omega-scan was performed, divided into frames of 0.1° rotation using 0.3 s integration time. The wavelength was tuned to 0.72931 Å. Data reduction, including Lorentz-Polarisation and absorption correction, was performed with X-ray detector software (XDS) [14]. The refinement of the lattice parameters was done with CrysAlis (Rigaku Oxford Diffraction, 2015). For the reconstruction of reciprocal space sections, a modified version of the software Xcavate [15] was utilised. Further details of the intensity data collection and crystal-structure refinement of rusinovite are reported in Table 1. Data about atom coordinates (x,y,z), occupancies, and equivalent isotropic displacement parameters (Uiso, Å2) (Table S1), as well as, anisotropic displacement parameters (Å2) (Table S2), the selected interatomic distances (Å) (Table S3) and cif file (Scheme S1) for rusinovite from Shadil-Khokh volcano, South Ossetia were reported in Supplementary materials.

Table 1. Parameters for X-ray data collection and crystal-structure refinement.

Crystal Data	
Chemical formula	$Ca_{10}(Si_2O_7)_3Cl_2$
Crystal system	orthorhombic
Space group	*Cmcm* (No. 63)
Unit-cell dimensions	a = 3.76330(4) Å
	b = 16.9423(3) Å
	c = 17.3325(2) Å
Unit cell volume	1105.10(4) Å^3
Formula weight	976.2
Density (calculated)	2.934 g/cm^3
Z	2
Crystal size	28 × 18 × 15 μm
Data collection	
Diffractometer	beamline X06DA, Swiss Light Source single-axis Aerotech goniometer, PILATUS 2M-F detector

Table 1. *Cont.*

Crystal Data	
Radiation wavelength	0.72931 Å
Detector to sample distance	80 mm
Oscillation range	0.1°
No. of frames measured	1800
Time of exposure	0.3 s
Reflection ranges	$-5 \leq h \leq 5$; $-25 \leq k \leq 23$; $-25 \leq l \leq 23$
Reflection measured	5015
R_{int}	0.0274
Refinement of structure	**full matrix least-squares on *F***
No. of unique reflections	1087
No. of observed unique refl. [*I* > 3s(*I*)]	1032
Final *R* values [*I* > 3s(*I*)]	$R = 0.021$; $wR = 0.035$
Final *R* values (all data)	$R = 0.022$; $wR = 0.036$
S (all data)	2.34
Refined parameters	85
Weighting scheme	$w = 1/(s^2(F) + 0.0001F^2)$
$\Delta\rho_{min}$ [e Å^{-3}]	-0.73
$\Delta\rho_{max}$ [e Å^{-3}]	0.32

4. Results

4.1. Chemical Composition and Raman Spectroscopy of Rusinovite

The chemical analysis of rusinovite from the two localities is listed in Table 2. A small loss of the chlorine content in rusinovite from Shadil-Khokh volcano can be caused by slight hydration or methodological problems of chlorine measurements [1].

Table 2. Chemical analysis of rusinovite from the Bellerberg and Shadil-Khokh volcanoes.

Component	Bellerberg Volcano					Shadil-Khokh Volcano				
	Mean 18					**Mean 14**				
	wt %	S.D.	Range	Atom	pfu	wt %	S.D.	Range	Atom	pfu
SiO$_2$	36.73	0.23	36.44–37.33	Si	6.00	36.89	0.23	36.12–36.93	Si	5.99
CaO	56.70	0.35	56.24–57.11	Ca	9.93	57.25	0.35	56.79–58.00	Ca	9.95
FeO	0.39	0.13	0.26–0.61	Fe	0.05	0.26	0.13	0.20–0.32	Fe	0.03
MgO	0.06	0.03	0.00–0.09	Mg	0.02	0.09	0.03	0.08–0.11	Mg	0.02
Cl	7.21	0.26	7.11–7.31	Cl	2.00	6.94	0.26	6.76–7.18	Cl	1.91
H$_2$O *	0.00					0.08			OH	0.08
–O=Cl	1.63					1.57				
Total	99.47					99.95				

* calculated on charge balance; S.D. = 1σ standard deviation.

The Raman spectra of the investigated rusinovite (Figure 4A,B) are similar to the spectrum from the holotype specimen. The most intense bands correspond to the vibrations of (Si$_2$O$_7$) group. The stretching motions of this group generally occur between 800 and 1100 cm^{-1}, and it can be differentiated into vibrations of SiO$_4$ (800–1000 cm^{-1}) and stretching vibrations of Si–O–Si bridges (1000–1100 cm^{-1}) [16]. A sharp, strong band at 905 cm^{-1} is related to the ν_1 symmetric stretching vibrations of Si$_2$O$_7$. The bands at 1041, 658 and 641, 365 cm^{-1} are attributed to the ν_3, ν_4, and ν_2, respectively. Galuskin [1] reported, that the rusinovite spectrum is highly similar to the spectrum of rankinite Ca$_3$Si$_2$O$_7$ [1]. The presence of a band doublet about 640 and 660 cm^{-1} linked to the symmetric

bending ν_4 (Si_2O_7) vibrations is characteristic for rusinovite. Bands occurring below 350 cm^{-1} are connected with Ca–O–Ca, O–Ca–O and librational vibrations of the Si_2O_7 group [1,17].
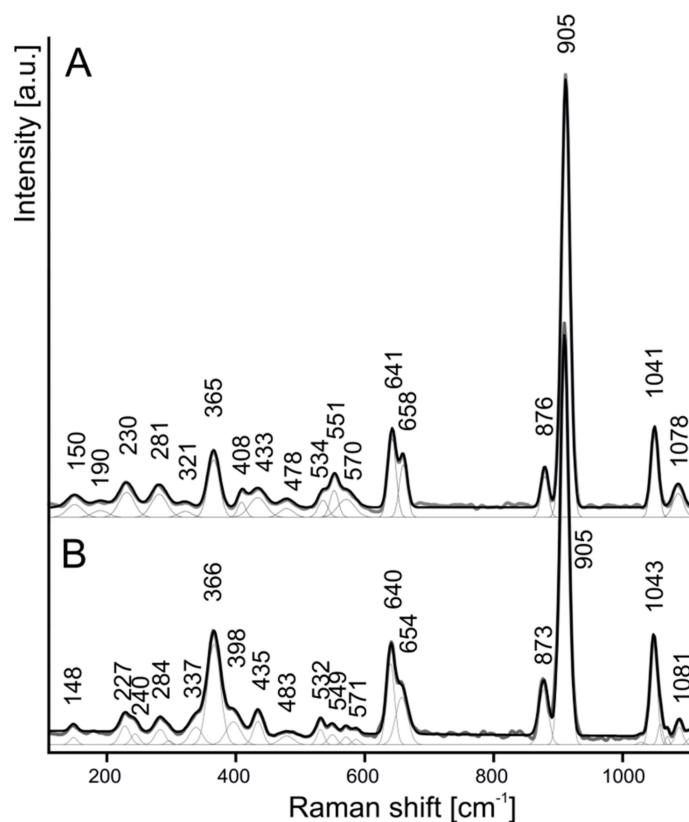

Figure 4. Raman spectra of rusinovite from (**A**) Shadil-Khokh volcano and (**B**) Bellerberg volcano.

4.2. Crystal Structure of Rusinovite

Rusinovite [1], as well as its synthetic analogue [6], exhibits columns of disordered disilicate groups. The first crystal structure refinement of the average structure of rusinovite from single-crystal data was reported by Galuskin et al. [1].

As the rusinovite crystals from the new locality (Shadil-Khokh volcano, South Ossetia) showed almost identical lattice parameters (Table 1) as reported before [1], we started the structure refinement from the known model. The refinement proves that the structures are basically the same. Final atom coordinates, anisotropic displacement parameters, as well as interatomic distances for rusinovite from Shadil-Khokh volcano can be found in a cif file (Supplementary Material).

The average crystal structure of $Ca_{10}(Si_2O_7)_3Cl_2$ consists of the Ca1- and Ca3-polyhedrons and two disilicate units, which form undulating layers perpendicular to **b** (Figure 5). The disilicate units appear to be "face-sharing" (Figure 6), which is an artifact of the disorder. In the real structure, only each second Si_2O_7 unit is occupied. The single layers are connected by the Ca2-site and Cl atoms. Chlorine atoms with characteristic distorted tetrahedral coordination are surrounded only by calcium ions. The bond lengths between Ca1–Cl and Ca2–Cl are within the range from 2.75Å to 2.92Å.
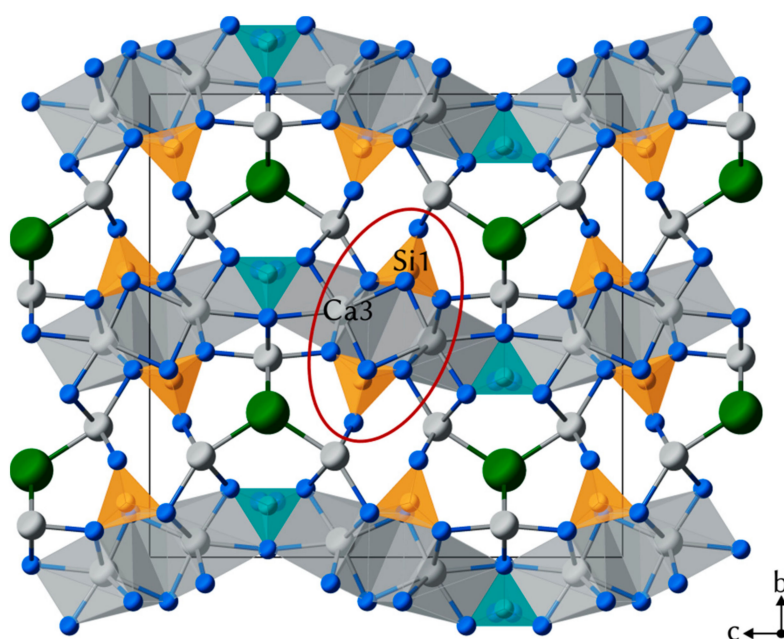
Figure 5. Crystal structure of rusinovite, projected along [100]. There are two types of Si_2O_7 disilicate units: Si1 and Si2 tetrahedra are light brown and greenish blue, respectively. Calcium atoms are shown as grey spheres and in addition, coordination polyhedra of Ca3 are depicted in grey. Oxygen atoms are presented as small blue spheres and Cl as green spheres.
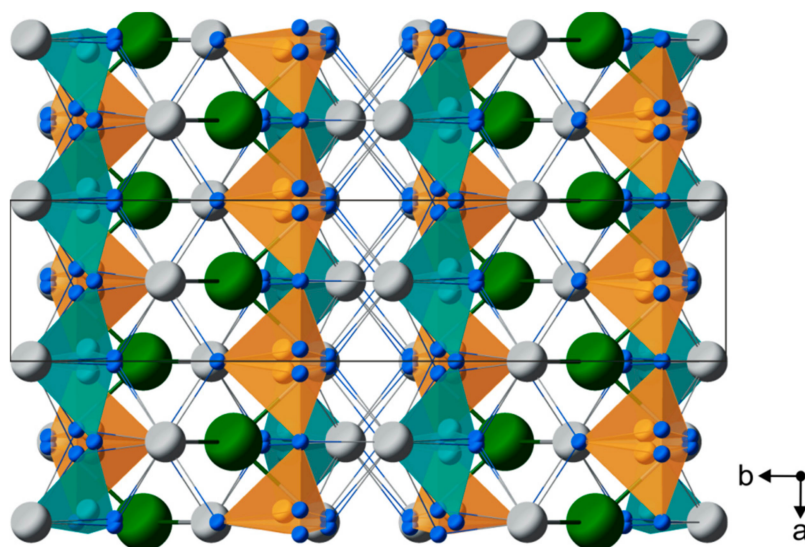

Figure 6. "Face-sharing" disilicates units appear in the average structure of rusinovite. The real structure exhibits ordered columns, where every second Si_2O_7 group is present.

In addition to the lattice formed by Bragg reflections, the diffraction pattern exhibits diffuse streaks which are parallel to **b*** and do not intersect any of the lattice nodes. The streaks are located at $h = 0.5, 1.5, 2.5 . . .$. Reciprocal space sections (*hkl*) with $l = 0, 1, 2, . . .$ show Bragg reflections and lines of diffuse scattering. Sections (*hkl*) at $h = 0.5, 1.5, 2.5, . . .$ exhibit rods of diffuse scattering only (Figure 7).
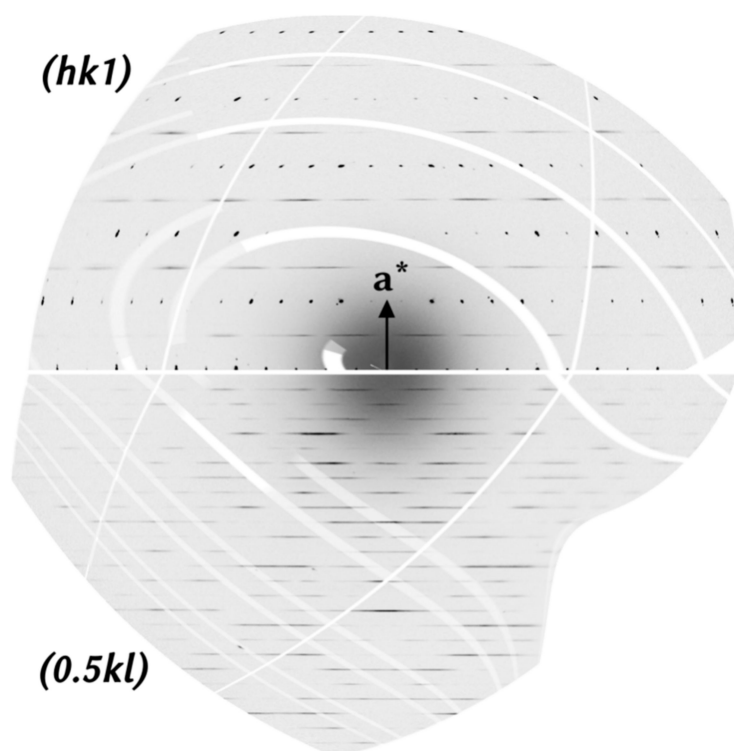
Figure 7. Layers of the reciprocal space of rusinovite as reconstructed from synchrotron diffraction data. Layer *hk1* (top half) exhibits Bragg reflections and diffuse lines parallel to **b***, whereas the layer (*0.5kl*) (lower half) shows only diffuse lines. In both images, **b*** is oriented horizontally parallel to the diffuse lines. The intensity scale (arb. units) was chosen to range from zero (white) to 60 (black) to show details of the weak diffuse intensities. For comparison, the intensities of the Bragg reflections in the upper half of the image range up to 12.5×10^3.

The observed pattern of diffuse lines proves the existence of stacking faults in rusinovite. The positions of the diffuse lines suggest that layers (parallel to the **a**, **c**-plane) are stacked along **b** with random disorder. The most likely mechanism is that within each layer the Si_2O_7 groups are ordered—which results in the doubling of the lattice parameter *a*—and thus creating two possible origins (along **a**) for each layer. The Si_2O_7 groups, which in the average structure appear to be disordered, are indeed ordered. Between neighboring columns of Si_2O_7 groups, strong correlations exist which create ordered layers.

Information on the relative arrangement of $Si1_2O_7$ groups may be obtained from bond-valence sum (BVS) calculations of the Ca3 atom, which connects to two neighboring $Si1_2O_7$ units (Figure 5). Ca3 is coordinated by eight oxygen atoms in the average structure. Two of them belong to the Si2 tetrahedra and their BVS contribution is independent of the two possible positions of the tetrahedra. The other six oxygen atoms are connected to two Si1-columns. These six atoms are split-atoms belonging to one of two possible positions of the $Si1_2O_7$ groups. Looking at the two neighboring $Si1_2O_7$ columns, there may be two different relative arrangements of the Si_2O_7 groups: Ladder-like (Si_2O_7 groups are side by side along **a**), or zig-zag-like (Figure 8). Taking these two arrangements into account, we must consider four different environments for Ca3: (1) includes bridging oxygen atoms (O3) of both columns (8-fold coordination), (2) no bridging O3 atom is included (6-fold coordination), (3) and (4) only one bridging O3 is coordinating Ca3 (7-fold coordination). In the ladder-like arrangement the environments (1) and (2) occur, whereas in the zig-zag-arrangement only (3) and (4) are possible. The BVS for (1) and (2) are 1.74 and 2.38, respectively. The zig-zag arrangement seems more likely as the corresponding BVS are 1.84 and 2.28 for the environments (3) and (4).

Correlations between the Si1 and Si2-columns are less obvious as neither Ca2 nor Ca1 have bridging oxygen atoms of both columns in their first coordination sphere. Additionally, distortions of the local structure may be involved.

A careful re-investigation of the original data used in [1], revealed that diffuse scattering is detectable, although very weak. The observation of diffuse streaks in X-ray rotation photographs [6] is consistent with our observation in rusinovite crystals. However, the doubled lattice parameter **c** (corresponds to **b** in the setting used by Hermoneit et al. [6]) is not observed in our data. However, this could be explained by a more complex order of disilicate groups within the layers.

A relation to the monoclinic cell (a = 18.66, b = 14.11, and c = 18.14 Å, β = 111.6°) described by Stemmermann et al. [4] seemingly does not exist. It is possible that the monoclinic cell corresponds to a polymorph, which has not yet been further characterized.
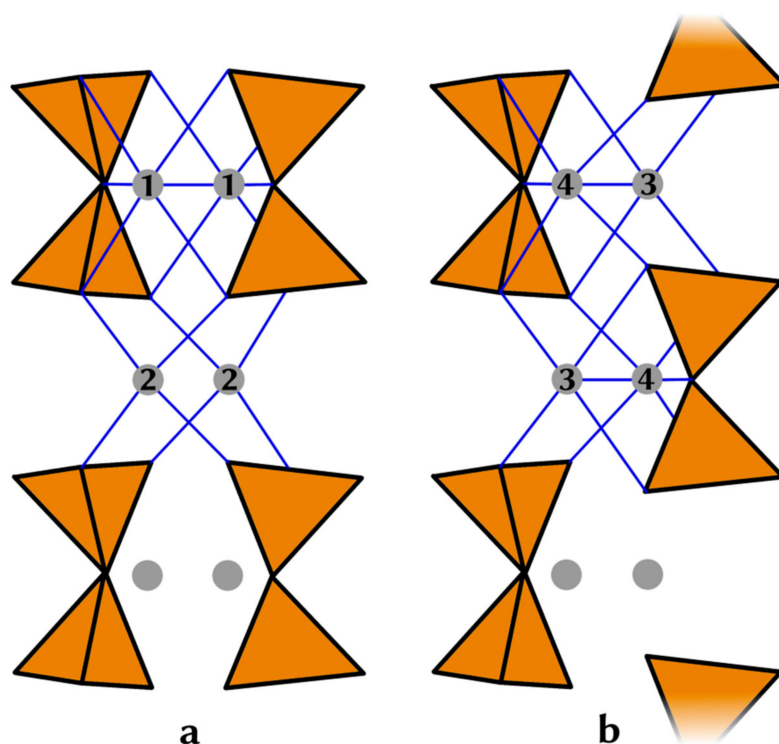
Figure 8. Two possible relative arrangements of neighboring "Si1$_2$O$_7$-columns" and resulting bonds of Ca3, projected along [011], the a-direction is vertical (the shown part of the structure is encircled in red in Figure 5). (**a**) shows a ladder-like arrangement, whereas in (**b**) the zig-zag arrangement is depicted. Bond valence sums for the resulting environments of Ca3 (1–4) are discussed in the text. Bonds from Ca3 to oxygen atoms of the Si2$_2$O$_7$-column are omitted.

5. Discussion

Rusinovite was previously found in South Ossetia [9] and at the Bellerberg volcano [18], but this study is a first mineralogical description of this mineral from these localities. The obtained chemical data are in good agreement with the composition of the holotype specimen from Chegem Caldera, Northern Caucasus, Russia [1]. An insignificant presence of Mg^{2+} and Fe^{2+} impurities at Ca site is characteristic for the studied samples. The Raman spectra of rusinovite from both localities are analogous to the one of the holotype rusinovite with a characteristic doublet about 640–660 cm^{-1} (Figure 4; [1]). In the Raman spectra of disilicates, the split of 640–660 cm^{-1} band was noted before [19]. It is connected with the change Si–O–Si angle [20] and suggests that two types of (Si$_2$O$_7$) groups with different Si–O–Si angles [1] exist in rusinovite.

One of the goals of this study was to check rusinovite for superstructure reflections, which have been reported for synthetic material [6]. Additional Bragg reflections were not observed, however diffuse scattering revealed that stacking faults of layers with doubled *a* are present. Ordered polytypes may exhibit larger periodicity in **b**, the doubling in **c** as suggested by Hermoneit et al. [6] is not explained. The new data does not show evidence for any significant correlation in the stacking sequence. The diffraction pattern can be fully explained by random stacking faults.

For the samples from South Ossetia, we were enabled to distinguish successive stages of mineral formation with a decrease of silica content towards the xenolith from volcanic rock. Minerals occurring in the subsequent zones are characterized by the variable Ca:Si ratio. Provisionally it is possible to distinguish the following successive metasomatic zones in the Shadil-Khokh xenolith: wollastonite/rankinite zone (also as endocontact zone), Ca:Si $\approx$ 1–1.5; larnite/cuspidine/rondorfite zone, Ca:Si $\approx$ 2:1; spurrite/Ca-humite zone, Ca:Si $\approx$ 2.33–2.5:1; and central marble zone (Figure 1C, [21]). In both, xenolith exo- and endocontact, the field of rusinovite prevalence is distinct and corresponds to a Ca:Si ratio between 1.5:1 and 2:1. This ratio is similar to the Ca:Si ratio of the rusinovite-bearing zone from the holotype locality [1,21].

The occurrence of rusinovite in the specific zones with characteristic Ca:Si ratio proves that its formation is a result of metasomatic processes, which require Si diffusion to Ca-bearing xenolith and Ca diffusion through a porous system of volcanic rock to endocontact zones (Figure 2). At the first stage chlorine-free minerals such as wollastonite or rankinite are formed [21]. Later, these minerals were affected by the flow of Cl-bearing fluids of volcanic origin, and as a result rusinovite was formed.

6. Conclusions

The rusinovite from the two new localities shows similar chemical composition and physical properties as the holotype specimen. The single-crystal synchrotron diffraction experiments on rusinovite from the Shadil-Khokh volcano did not confirm the presence of a superstructure as observed in its synthetic analogue. However, the measured one-dimensional diffuse scattering revealed more details of the stacking fault mechanism.

Rusinovite genesis is connected with metasomatic processes, which occurred at the contact zones of the xenolith and volcanic rock.

Author Contributions: D.Ś., R.J., H.K. and I.G. wrote the paper, D.Ś. performed the mineralogical and petrological investigations and Raman studies, R.J., H.K. and B.K. performed investigation of rusinovite structure, V.G. collected the samples.

References

1. Galuskin, E.V.; Galuskina, I.O.; Lazic, B.; Armbruster, T.; Zadov, A.E.; Krzykawski, T.; Banasik, K.; Gazeev, V.M.; Pertsev, N.N. Rusinovite, $Ca_{10}(Si_2O_7)_3Cl_2$: A new skarn mineral from the Upper Chegem caldera, Kabardino-Balkaria, Northern Caucasus, Russia. *Eur. J. Mineral.* **2011**, *23*, 837–844. [CrossRef]
2. Galuskin, E.V.; Galuskina, I.O.; Kusz, J.; Gfeller, F.; Armbruster, T.; Bailau, R.; Dulski, M.; Gazeev, V.M.; Pertsev, N.N.; Zadov, A.E.; et al. Mayenite supergroup, part II: Chlorkyuygenite from Upper Chegem, Northern Caucasus, Kabardino-Balkaria, Russia, a new microporous mineral with "zeolitic" H_2O. *Eur. J. Mineral.* **2015**, *27*, 113–122. [CrossRef]
3. Gfeller, F.; Armbruster, T.; Galuskin, E.V.; Galuskina, I.O.; Lazic, B.; Savelyeva, V.B.; Zadov, A.E.; Dzierżanowski, P.; Gazeev, V.M. Crystal chemistry and hydrogen bonding of rustumite $Ca_{10}(Si_2O_7)_2(SiO_4)(OH)_2Cl_2$ with variable OH, Cl, F. *Am. Mineral.* **2013**, *98*, 493–500. [CrossRef]
4. Stemmermann, P.; Pöllmann, H. The system $CaO-SiO_2-CaCl_2$-phase equilibria and polymorphs below 1000 °C. An interpretation on garbage combustion ashes. *Neues Jahrb. Mineral. Monatsh.* **1992**, *9*, 409–431.
5. Chesnokov, B.V.; Vilisov, V.; Bushmakin, A.; Kotlyarov, V.; Belogub, E.V. New minerals from a fired dump of the Chelyabinsk coal basin. *Ural Mineral. Zbor.* **1994**, *3*, 3–34.
6. Hermoneit, B.; Ziemer, B.; Malewski, G. Single crystal growth and some properties of the new compound $Ca_3Si_2O_7 \cdot 13CaCl_2$. *J. Cryst. Growth* **1981**, *52*, 660–664. [CrossRef]
7. Ding, W.; Wang, J.; Zhang, M.; Zhang, Q.; Su, Q. Luminescence properties of new $Ca_{10}(Si_2O_7)_3Cl_2:Eu^{2+}$ phosphor. *Chem. Phys. Lett.* **2007**, *435*, 301–305. [CrossRef]
8. Gazeev, V.M.; Gurbanova, O.; Zadov, A.E.; Gurbanov, A.G.; Leksin, A. Mineralogy of skarned carbonate xenoliths from Shadil-Khokh volcano (Kelski Vulcan area of Great Caucasian Range). *Vestn. Vladikavkazskogo Nauchnogo Cent.* **2012**, *2*, 18–27.
9. Gfeller, F.; Środek, D.; Kusz, J.; Dulski, M.; Gazeev, V.; Galuskina, I.; Galuskin, E.; Armbruster, T. Mayenite supergroup, part IV: Crystal structure and Raman investigation of Al-free eltyubyuite from the Shadil-Khokh volcano, Kel' Plateau, Southern Ossetia, Russia. *Eur. J. Mineral.* **2015**, *27*, 137–143. [CrossRef]
10. Mihajlovic, T.; Lengauer, C.L.; Ntaflos, T.; Kolitsch, U.; Tillmanns, E. Two new minerals, rondorfite, $Ca_8Mg[SiO_4]_4Cl_2$, and almarudite, $K(\square,Na)_2(Mn,Fe,Mg)_2(Be,Al)_3[Si_{12}O_{30}]$, and a study of iron-rich wadalite, $Ca_{12}[(Al_8Si_4Fe_2)O_{32}]Cl_6$, from the Bellerberg (Bellberg) volcano, Eifel, Germany. *Neues Jahrb. Mineral. Abh.* **2004**, *179*, 265–294.
11. Hentschel, G. Mayenit, $12CaO-7Al_2O_3$, und Brownmillerit, $2CaO-(Al, Fe)_2O_3$, zwei neue Minerale in den Kalksteineinschlussen der Lava des Ettringer Bellerberges. *Neues Jahrb. Mineral. Mh.* **1964**, 22–29. (In German)
12. Galuskin, E.V.; Gfeller, F.; Galuskina, I.O.; Armbruster, T.; Bailau, R.; Sharygin, V.V. Mayenite supergroup, part I: Recommended nomenclature. *Eur. J. Mineral.* **2015**, *27*, 99–111. [CrossRef]
13. Schlüter, J.; Malcherek, T.; Pohl, D.; Schäfer, C. Vondechenite, a new hydrous calcium copper chloride hydroxide, from the Bellerberg, East-Eifel volcanic area, Germany. *Neues Jahrb. Mineral.* **2018**, *195*, 79–86. [CrossRef]
14. Kabsch, W. XDS. *Acta Crystallogr. D* **2010**, *66*, 125–132. [CrossRef] [PubMed]
15. Estermann, M.A.; Steurer, W. Diffuse scattering data acquisition techniques. *Phase Transit.* **1998**, *67*, 165–195. [CrossRef]
16. Le Cleac'h, A.; Gillet, P. IR and Raman spectroscopic study of natual lawsonite. *Eur. J. Mineral.* **1990**, *2*, 43–53. [CrossRef]
17. Dulski, M.; Bulou, A.; Marzec, K.M.; Galuskin, E.V.; Wrzalik, R. Structural characterization of rondorfite, calcium silica chlorine mineral containing magnesium in tetrahedral position $[MgO_4]^{6-}$, with the aid of the vibrational spectroscopies and fluorescence. *Spectrochim. Acta. A. Mol. Biomol. Spectrosc.* **2013**, *101*, 382–388. [CrossRef] [PubMed]
18. Galuskin, E.V.; Krüger, B.; Krüger, H.; Blass, G.; Widmer, R.; Galuskina, I.O. Wernerkrauseite, $CaFe^{3+}_2Mn^{4+}O_6$: The first nonstoichiometric post-spinel mineral, from Bellerberg volcano, Eifel, Germany. *Eur. J. Mineral.* **2016**, *28*, 485–493. [CrossRef]
19. Lazarev, A.N. *Vibrational Spectra and Structure of Silicates*; Consultants Bureau: New York, NY, USA, 1972.

20. McMillan, P. Structural studies of silicate glasses and melts—applications and limitations of Raman spectroscopy. *Am. Mineral.* **1984**, *69*, 622–644.

21. Galuskina, I.O.; Krüger, B.; Galuskin, E.V.; Armbruster, T.; Gazeev, V.M.; Włodyka, R.; Dulski, M.; Dzierżanowski, P. Fluorchegemite $Ca_7(SiO_4)_3F_2$, a new mineral from the edgrewite-bearing endoskarn zone of an altered zenolith in ignimbrites from Upper Chegem caldera, Northern Caucasus, Kabardino-Balkaria, Russia: Occurrence, crystal structure and new data on the mineral assemblages. *Can. Mineral.* **2015**, *53*, 325–344. [CrossRef]